Particuology 91 (2024) 155–167

Contents lists available at ScienceDirect

Particuology

journal homepage: www.elsevier.com/locate/partic

Effect of reaction and post-treatment conditions on physico-chemical properties of magnetic iron oxide nano-particles

Masome Moeni [a], Mohamed Edokali [a], Matthew Rogers [b], Oscar Cespedes [b], Louey Tliba [a], Tamseela Habib [a, c], Robert Menzel [d], Ali Hassanpour [a, *]

[a] School of Chemical and Process Engineering, Faculty of Engineering and Physical Science, University of Leeds, Leeds, LS2 9JT, UK
[b] School of Physics and Astronomy, Faculty of Engineering and Physical Science, University of Leeds, Leeds, LS2 9JT, UK
[c] Mechanical Engineering Department, University of Engineering & Technology, Lahore, Pakistan
[d] School of Chemistry, Faculty of Engineering and Physical Science, University of Leeds, Leeds, LS2 9JT, UK

ARTICLE INFO

Article history:
Received 24 November 2023
Received in revised form
2 February 2024
Accepted 21 February 2024
Available online 16 March 2024

Handling Editor: Lifang Wu

Keywords:
Iron oxide nanoparticles
Co-precipitation
Stability
Aggregation
Magnetic properties

ABSTRACT

Poor stability and dispersibility, as well as aggregation are considered as major challenges in clinical application of iron oxide nanoparticles (IONPs). Several studies have shown that the synthesis parameters and post-synthesis treatments e.g., drying methods, have the capability to improve the particles' characteristics. Herein, we investigate the combined effect of synthesis and post-treatment parameters on the particle size, stability and magnetism of IONPs. Magnetite (Fe_3O_4) NPs were prepared via co-precipitation and post-treated using different methods, i.e. (i) freeze dried at −53 °C, 0.133 mbar for 48 h (liquid nitrogen frozen (LFD) and freezer frozen (FFD)), (ii) vacuum oven dried (VOD) at 60 °C for 24 h, and (iii) kept wet colloidal (WET), dispersed in deionized water. The Fe_3O_4 NPs' chemical functional groups, size, shape, crystallinity, stability, aggregation, porosity, and magnetic properties were further analysed using different characterisation techniques. Analytical results showed that, while the WET sample had the best stability and significantly less aggregation at different temperatures, amongst post-treated Fe_3O_4 NPs, LFD sample exhibited the best stability (up to 37 °C), dispersion and smallest polydispersity index. Furthermore, all dried NPs had superparamagnetic characteristics, while, LFD Fe_3O_4 NPs had better magnetic properties and stability than other drying methods.

1. Introduction

Fabrication of iron oxide nanoparticles (IONPs) has been extensively investigated by numerous researchers in the field of nanotechnology for different applications. In this regard, hematite (α-Fe_2O_3), maghemite (Υ-Fe_2O_3), magnetite (Fe_3O_4) IONP species have been extensively scrutinised across a wide range of fields, particularly, in clinical utilization e.g., targeted drug delivery (TDD), as a contrast medium in magnetic resonance imaging, as heat mediator in magnetic hyperthermia or as biosensor probes (Chen, Cheng, et al., 2021; Priyadarshi et al., 2021; Zhao et al., 2023), etc. In particular, Fe_3O_4 NPs have been mostly investigated because of their exclusive traits such as low solubility in most solvents, chemical stability, outstanding magnetic properties, and high saturation field, accessibility, and tunability (Novoselova, 2021). Fe_3O_4 has a cubic inverse spinel crystal structure and the space group of Fd $\overline{3}$ m, that is composed of thirty-two oxygen atoms in a face-centred-cubic (fcc) closed packing in which the iron (II) cation occupies half of the octahedral sites while iron (III) cation resides in the other half and also occupies the whole tetrahedral lattice site. The fcc close packing permits the Fe-O atoms to have strong interactions with other atoms, and also to have an energetically stable structure (Mahmoudi et al., 2011). Fe_3O_4 is an amphoteric solid, with Fe-OH surface sites being able to undergo protonation/deprotonation reactions, depending on the reaction/processing conditions. Moreover, Fe_3O_4 has a tendency for isomorphic substitutions in which, one cation can be replaced with another similar sized cation, providing additional, permanent surface charge for the Fe_3O_4 nanoparticles (NPs). Therefore, the colloidal stability of Fe_3O_4 NPs is highly driven by electrostatic repulsion and can be

* Corresponding author.
E-mail address: A.Hassanpour@leeds.ac.uk (A. Hassanpour).

https://doi.org/10.1016/j.partic.2024.02.006

Abbreviation

API	Active pharmaceutical ingredients
ATR	Attenuated total reflection
BET	Brunauer–Emmett–Teller
DDS	Drug delivery system
DLS	Dynamic light scattering
EDX	Energy dispersive X-ray spectroscopy
XMF	External magnetic field
Fcc	Face-centred-cubic
FT-IR	Fourier transform infrared spectroscopy
FD	Freeze dry
FFD	Freezer frozen-freeze dry
HPLCW	High-Performance Liquid Chromatography grade water
D_H	Hydrodynamic size
II	Instability index
IONPs	Iron oxide nanoparticles
LFD	Liquid nitrogen frozen-freeze dry
NA	No aging
NPs	Nanoparticles
SCM	Superconducting magnet
TDD	Targeted drug delivery
Temp	Temperature
TEM	Transmission electron microscopy
VOD	Vacuum oven dry
VDr	Vacuum desiccator
VSM	Vibrating sample magnetometer
WET	Wet colloidal
XRD	X-ray diffraction
ZP	Zeta potential
ZFCFC	Zero-field cooled, and field cooled

further enhanced by NP functionalisation to induce additional steric stabilisation (Demangeat et al., 2018; Vindedahl et al., 2016).

The utilization of Fe_3O_4 NPs for TDD relies on two important factors, including size and magnetization effect (Chomoucka et al., 2010). The modifications of size by altering the synthesis parameters can tune the saturation magnetization of Fe_3O_4 NPs. Perceptibly, their superparamagnetic properties are fundamental features of Fe_3O_4 NPs in TDD since it permits the navigation of Fe_3O_4 NPs within the body *via* an external magnetic field (XMF), at the same time after switching off XMF the NPs do not maintain any residual magnetism leading to their dispersion (Das et al., 2020). Dong et al. (Dong et al., 2016) demonstrated that regulating the concentration of iron ions in one-pot-synthesis can generate Fe_3O_4 NPs with a size between 67 nm and 143 nm which resulted in the rise of the saturation magnetization from 63.0 emu/g to 68.9 emu/g (Dong et al., 2016). In another study, elevating the temperature from 18 °C to 80 °C caused the size of the particles to decrease from 120 nm to 20 nm, resulting in a reduction of the saturation magnetization from 81.7 emu/g to 71.0 emu/g. In addition, they reported at the optimal synthesis temperature of 60 °C stable Fe_3O_4 NPs with 25 nm size and saturation magnetization of 82.8 emu/g were generated (Chen, Ilyas, et al., 2021). As Fe_3O_4 NPs' unique behaviour undisputedly depends on their size, morphology and surface chemistry, the preparation pathways must be as reproducible as possible (Mihai et al., 2020; Shaoqiang et al., 2018). There are numerous synthesis pathways, conventional and emerging technologies, including hydrothermal, co-precipitation, thermal decomposition, microwave assisted, gas phase flame synthesis, bacteria/fungi mediated, and microfluidic methodologies (Yang et al., 2022). Amongst these synthesis pathways, the conventional one-pot co-precipitation is the most common route to produce nano-scale and highly magnetised Fe_3O_4 NPs, due to its simplicity (Ba-Abbad et al., 2022; Saragi et al., 2018). However, in a poorly controlled co-precipitation reaction nucleation and growth steps may develop intermittently, leading to aggregation and Ostwald ripening (Kregar et al., 2020; Wu et al., 2022). Smaller NPs that have higher surface energy may decompose and precipitate on larger NPs to obtain thermodynamically stable state in which the surface to area ratio will be lessened. This may result an undesirable size increase or wide size distribution, which is commonly known as Ostwald ripening (Gommes, 2019; Kregar et al., 2020; Rinkel et al., 2014). Reaction conditions such as prolonged reaction time, low pH and high temperature could lead to the formation of irregular sized NPs that may support the dominant growth of Ostwald ripening. (Fadli et al., 2017). Darminto et al. (Darminto et al., 2011) reported that at low pH the crystallite sizes of Fe_3O_4 NPs were larger due to Ostwald ripening (Darminto et al., 2011).

In manufacturing of active pharmaceutical ingredients (API), stability is one of the key aspects that have an impact on API quality (Boukoufi et al., 2022), and plays a vital part in a drug delivery system (DDS). Stability refers to the ability of pharmaceutical agent to preserve its integrity and the same feature from the time of its formulation throughout the storage until it reaches the site of interest in biological cells/tissue (Shah et al., 2020). Factors that should be considered for the formulation of magnetic nano DDS are chemical and physical instabilities, such as chemical reactions or drug leakages during storage (Abdelwahed, Degobert, Stainmesse, & Fessi, 2006; Franzé et al., 2018), solubility, dispersion and aggregation (Majeed et al., 2013). Keeping MNPs in aqueous form might help with their colloidal stability, however, this depends on concentration and intrinsic behaviour of the particles in an aqueous suspension (Demangeat et al., 2018). It was reported that the long-term storage of the magnetic pharmaceutical agents in aqueous form may often be insufficient for practical application, since the particles suspended in the aqueous solution could become unstable and prone to agglomeration over longer time scales. A common cause for instability issues, is the hydrolysis action of water that can break down the polymer coating of IONPs, causing drug leakage, then either leads to undesirable degradation or early elimination from the blood system (Lemoine et al., 1996). In some other studies, as described below, it has been suggested that the conversion of nano-suspensions into solid form during post-synthesis processes can also lead to instability issues during IONPs re-dispersion (Abdelwahed, Degobert, Stainmesse, & Fessi, 2006; Aisida et al., 2020; Camacho et al., 2018; Chen et al., 2016; Mpelane et al., 2022; Nanda et al., 2014; Pinto et al., 2018). Therefore, to identify the key attributes of physico-chemical instabilities of Fe_3O_4 NPs, the most common post-synthesis treatment methods of freeze drying and vacuum oven drying are reviewed in the following.

Vacuum oven is one of the most common and fastest drying procedure utilized in industry and academia. Aisida et al. (Aisida et al., 2020) reported the Fe_3O_4 NPs dried in vacuum oven at 60 °C, had particle size of 18-19 nm (as measured by scanning electron microscopy (SEM)) and superparamagnetic characteristic with saturation magnetization of 72.07 emu/g (Aisida et al., 2020). Lyophilisation/Freeze drying is the process of eliminating water from the frozen sample *via* sublimation. It was developed to enhance the stability and improve the shelf life and storage of pharmaceutics (Tang et al., 2004) and only started to gain attention after 1990s due to the increased application of biological materials,

e.g., protein (Park, 2017). Drying procedure can cause physical structural changes, such as porosity (Joardder et al., 2016). The porosity can have an impact on physico-chemical properties of Fe_3O_4 NPs and increase the surface area to volume ratio for high drug loading capacity or adsorption effects (Pinto et al., 2018). In this respect, Mpelane et al. (Mpelane et al., 2022) studied the adsorption of levofloxacin onto mesoporous IONPs. The author reported that the surface adsorption and inter-particle diffusion drove the adsorption of levofloxacin to the mesoporous IONPs (Mpelane et al., 2022). Numerous studies have shown that lyophilisation can generate porous scaffolds without the need for toxic chemicals or further synthesis pathways (Camacho et al., 2018; Chen et al., 2016; Nanda et al., 2014). Yang et al. (Yang et al., 2017) designed a simple method to prepare an atelocollagen/gelatin sponge via lyophilisation instead of using toxic chemical solvents. The study demonstrated that the formation of ice crystals during the sublimation influenced the size and shape of the formed pores. Therefore, any condition such as freezing time/temperature and concentration of media have an impact on generation of ice crystals, consequently, determines the structure of the pores, for instance, the freezing temperature above −30 °C expanded pore size (Yang et al., 2017). In addition, conditions; including freezing and drying temperatures, pressure, formulation of the material, annealing procedure at which materials are subjected, can induce desiccation or freezing stresses with destructive consequences to the stability of NPs (Abdelwahed, Degobert, & Fessi, 2006).

Despite an extensive reported work in the literature, to the best of our knowledge, there are no studies on comparing the synergistic effects of synthesis conditions such as pH, temperature, solvent, and post-synthesis treatments (e.g. liquid nitrogen freeze drying (LFD), freezer frozen freeze drying (FFD), vacuum oven drying (VOD) and wet colloidal (WET) suspension with no drying) on the stability, magnetic and physico-chemical properties of Fe_3O_4 NPs. Furthermore, there is a lack of understanding the influence of post-treatment temperature, resembling conditions during storage and preparation for administration (ambient) and in vivo (normal tissues and tumour), on the abovementioned properties. Therefore, here, the material physico-chemical characteristics inherent to the aforementioned synthesis and post-synthesis procedures were systematically explored. To this end, IONPs were produced via a well-known precipitation synthesis at different synthetic conditions (different pH, different solvent compositions), and, crucially, at different post-synthetic processing conditions (freeze drying, vacuum oven drying, colloidal dispersion). The structural (e.g., particle size, surface area, porosity) and chemical (e.g., elemental composition, surface charge) properties of the resulting Fe_3O_4 NPs were comprehensively characterised through a wide range of analytical techniques (including Fourier transform infrared spectroscopy (FT-IR), nitrogen adsorption, Dynamic light scattering (DLS), SEM, Energy dispersive X-ray spectroscopy (EDX), and then linked to application-relevant performance parameters, such as magnetic properties and re-dispersion stability.

2. Experimental

2.1. Material

Anhydrous iron (III) chloride ($FeCl_3$, AR grade), iron (II) sulfate heptahydrate ($FeSO_4 \bullet 7H_2O$, AR grade), and ammonium hydroxide (NH_4OH 25−30 wt%; AR grade, for adjusting pH) were purchased from Sigma-Aldrich, UK. Ethanol (70%, AR grade) and High-Performance Liquid Chromatography grade water (HPLCW) were purchased from VWR International Ltd, UK.

2.2. Synthesis of Fe_3O_4 nanoparticles

The synthesis method for preparing Fe_3O_4, partially adapted from the reported literatures (Antarnusa et al., 2020; Shalaby et al., 2020; Shirzadi et al., 2020), and is presented in Fig. 1. In brief, fixed amounts of $FeCl_3$ (2.892 g) and $FeSO_4 \bullet 7H_2O$ (1.473 g), with the molar ratio of 2:1, were dissolved in water (40 mL) with two different cases of (i) with adding ethanol (10 mL) and (ii) without adding ethanol. Sonicator was applied to homogenise the solution, then it was placed on a heat mantle stirrer, and vigorously stirred (800 rpm) for 45 min at two different temperatures of (i) 80 °C and (ii) 25 °C under reflux condition in an inert environment. NH_4OH was added to adjust pH (it was varied from 9.5 to 11), and induce precipitation at different basic reaction conditions. Each batch was prepared with aging (1 h) and without aging (no aging, NA) once it reached the desired pH. The samples were rinsed with ethanol and water (2:1) few times and several times with HPLCW only. The NPs were collected by centrifuge (10000 rpm, 40 min, 25 °C) followed by a permanent magnet. After final decantation, each batch then was divided into four equal sub-batches for different post-synthesis treatments: (i) frozen by liquid nitrogen for 20 min then placed in freeze dryer for 48 h (LFD), (ii) frozen in the freezer at −4 °C for 12 h then freeze dried for 48 h (FFD), (freeze drying condition; −53 °C and pressure of ~0.133 mbar), (iii) placed into a vacuum oven at 60 °C for 24 h (VOD), (iv) keeping the sample dispersed in HPLCW and stored in a fridge at (1 °C) (WET). Fig. 2 schematically illustrates the post-synthesis treatment of the as-synthesised Fe_3O_4 NPs.

2.3. Characterisation

FT-IR (Thermo Fisher Scientific Nicolet^{TM} iS10 spectrometer applying the attenuated total reflection (ATR)) at room temperature was employed to identify the functional groups of the as-synthesised Fe_3O_4 NPs in the range of 4000−400 cm^{-1}, at resolution of 32 cm^{-1} and 64 scans. The spectra were collected in the percentage of transmittance. The structural and crystal phase analysis of the Fe_3O_4 nanoparticles were investigated by Bruker D2 Phaser X-ray diffractometer with Cu-Kα radiation ($\lambda = 1.541$ Å) equipped with a Lenxeye detector. The operating voltage was at 30 kV and with an applied current of 10 mA. All the samples scanned in the angular range of $5° \leq 2\theta \leq 80°$ and exposure time of 10 s and total measurement time of 11 h. The average crystallite size was calculated from the obtained XRD data using the Scherrer equation. The surface morphologies and elemental composition of the Fe_3O_4 NPs were assessed, using a FEI TECNAI TF20: FEG-TEM Field emission gun TEM/STEM fitted with HAADF detector (Oxford Instruments INCA 350 EDX system/80 mm X-Max SDD detector and Gatan Orius SC600A CCD camera). The morphology of the Fe_3O_4 NPs was assessed by Hitachi SU8230, high performance cold field emission (CFE) scanning electron microscopy (SEM). The surface area and porosity of the dry powder Fe_3O_4 NPs were measured by Brunauer-Emmett-Teller (BET) gas adsorption/desorption using Micromeritics Tristar-3000 surface area and porosity analyser. The measurements were performed by initially degassing the NPs overnight at 200 °C. The synthesised Fe_3O_4 NPs were explored using the Zetasizer (Nano ZSP ZEN5600, Malvern Instruments Ltd, UK) to inspect the hydrodynamic size (D_H) and colloidal stability (zeta potential measurements) in the solutions. The Fe_3O_4 NPs dispersed in HPLCW were homogenised by Fisher Scientific Model FB705 ultra-sonic probe and then transferred into a disposable cuvette for examination. Dispersion Analyser (LUMiSizer LUM GmbH, Germany) was used to measure the stability of the dispersed Fe_3O_4 NPs in HPLCW at different temperatures. The magnetic properties of the powder Fe_3O_4 NPs were measured using a Quantum Design MPMS3 superconducting quantum interference

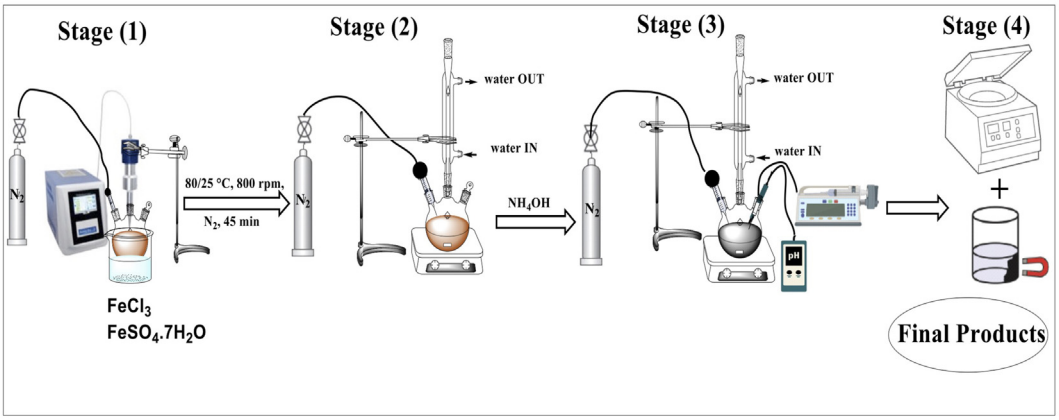

Fig. 1. Schematic illustration of the chemical reaction of the as-synthesised Fe_3O_4 NPs.

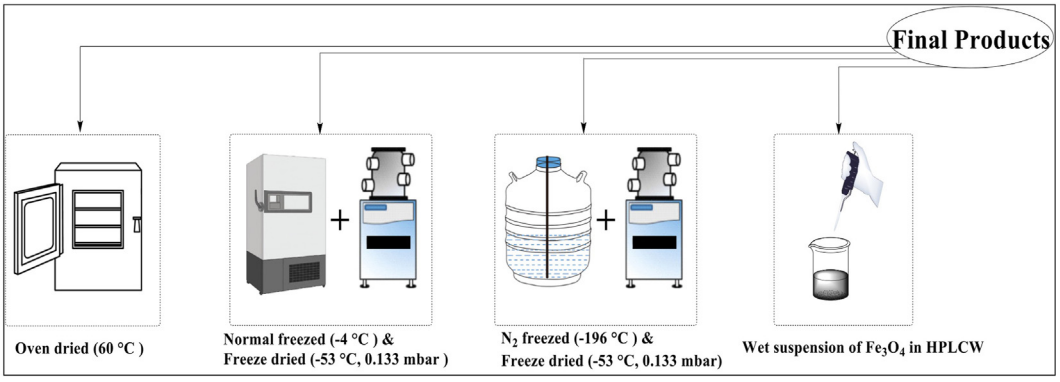

Fig. 2. Schematic illustration of the post-synthesis treatment of the as-synthesised Fe_3O_4 NPs.

device-vibrating sample magnetometer (SQUID-VSM) at 300 K, and magnetic field of 7 T.

3. Results and discussion

The effect of synthesis process conditions (pH, temperature, ethanol content and aging) and post-treatment methods on the hydrodynamic size (D_H) and instability index (II) of synthesised Fe_3O_4 NPs are collected in Fig. 3.

Prior to investigating the effect of the synthesis and the post-synthesis treatments of Fe_3O_4 NPs, factors such as the intrinsic magnetic characteristics, surface chemistry and van der Waals Forces were taken into consideration, as these can be the major contributors of particles' aggregation. Also, washing, centrifugation and magnetic collection processes can potentially initiate over-oxidation, aggregation or agglomeration. In washing step, to obtain a highly pure final Fe_3O_4 NPs and to prevent overoxidation, once the reaction finished, the solvents were decanted. Fresh ethanol and water were added to the flask and the particles were left dispersed in overnight under N_2 environment. The sample was then transferred into a centrifuge followed by further rinsing steps. The centrifugation condition (duration and speed) was optimised since the mechanical forces and agitation could potentially result in nanoparticles collision and aggregate.

Moreover, as it can be observed in Fig. 3, Fe_3O_4 NPs synthesised at low temperature (25 °C) had a higher instability index (II>2) and significant particle aggregation for all other synthesis and post-treatment conditions. SEM images are provided in the electronic Supplementary Fig. S1(a). According to the literature (Mascolo et al., 2013), this could be as a result of slow or incomplete reaction between Fe^{2+} and Fe^{3+} ions at a low temperature. Similarly, high instability index (II>2) results obtained for Fe_3O_4 NPs prepared at relatively mild basic conditions (pH 9.5 and pH 10) and high temperature (80 °C). This could potentially be attributed to the faster charge neutralisation between acidic Fe^{2+} and Fe^{3+} precursors (pH 1.1) and basic NH_4OH during the synthesis at high temperature which caused the particles to sediment rapidly and agglomerate (Godymchuk et al., 2019). Therefore, low pH (pH 9.5 and pH 10) and high temperature (80 °C) may have influenced the reaction kinetics, particles nucleation and growth rate which led to wider size distribution and Ostwald ripening phenomena.

Moreover, high temperature (80 °C), high pH (pH 11), and the absence of ethanol during the first step of synthesis led to high instability index for all other process and post-treatment conditions. In addition, it was noted that in the absence of ethanol, not only higher amount of NH_4OH was required to reach the desired pH but also the hydrolysis of $FeCl_3$ in water was more pronounced. Meanwhile, the use of ethanol had a positive effect on the particles D_H (smaller D_H value) and instability index (below 1). The findings were parallel with the literature where it was reported, the presence of ethanol can influence the oxidation rate and dissolution of iron salts, hence it can control the nucleation and particle growth producing monodisperse Fe_3O_4 NPs (Dang et al., 2009). In addition to, it was observed that the elevated temperature (80 °C) of the reaction enhanced the solubility of iron precursors accelerating the rate of nucleation and particles growth, forming particles with uniform size distribution. The elevated temperature may have facilitated extra thermal energy which overcame attractive forces

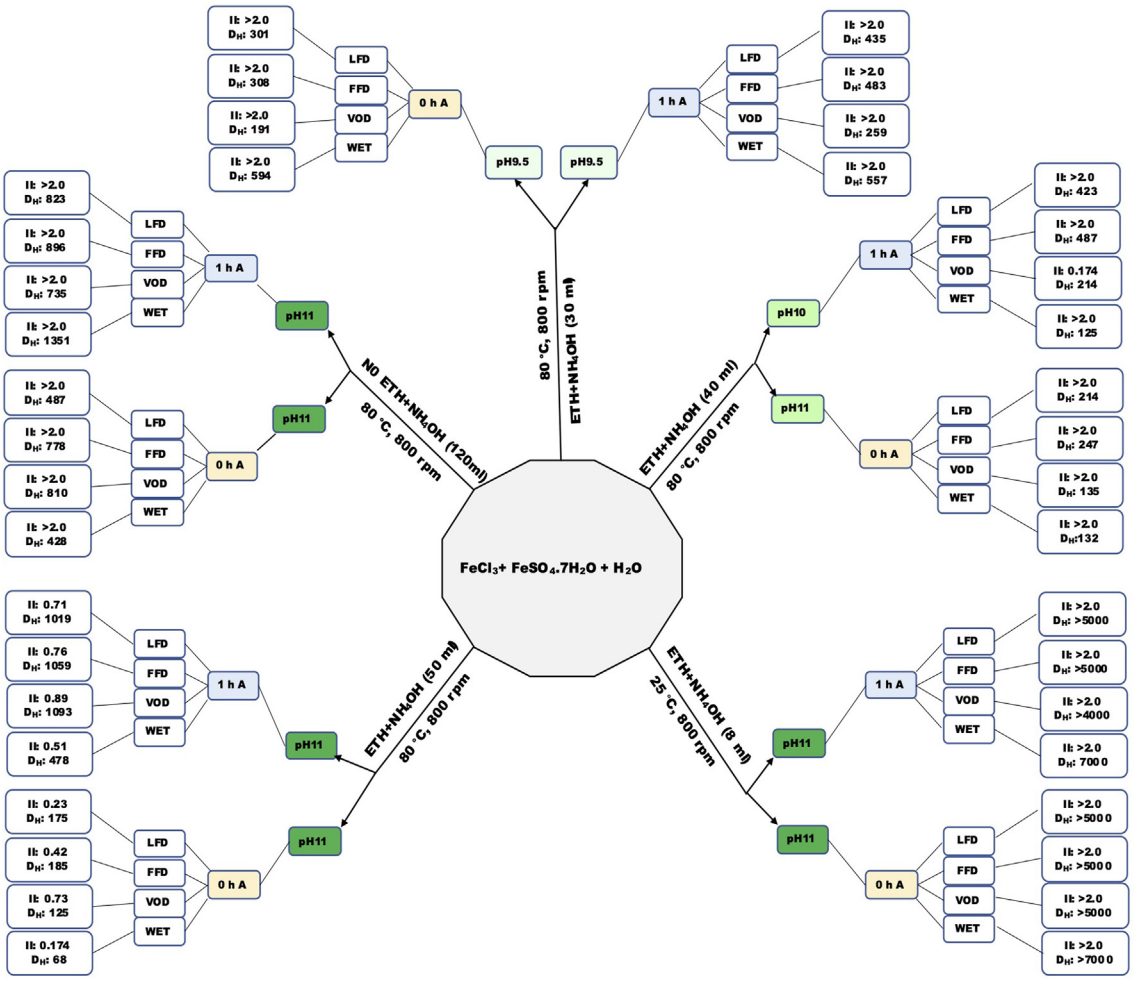

Fig. 3. Preparation pathways of Fe_3O_4 NPs at different process conditions and post-synthesis treatments together with the hydrodynamic size (D_H), and instability index (II).

and prevented them from drawing the NPs together and causing aggregation. These findings are in line with the findings in other studies (Chen, Ilyas, et al., 2021; Mascolo et al., 2013). Additionally, it is postulated that the formed Fe_3O_4 NPs at high pH will have Fe-OH groups (negatively charged) on their surface which can be deprotonated at high pH to Fe-O leading to better electrostatic stabilisation and overcoming the aggregation. The samples prepared at high temperature (80 °C), high pH (11) with no aging and the use of ethanol generated highly homogenous NPs system with decreased likelihood of Ostwald ripening. While, aging the same sample for 1 h after reaching the desirable pH, negatively impacted the instability index and D_H, causing agglomeration for all post-treatment methods. The Ostwald-ripening phenomenon can explain the enlargement of particle size at prolonged reaction time (aging 1 h) (Baojun Liu and Zhao, 2020; Yusoff et al., 2018). Plus, as particles start to co-precipitate and grow, they may undergo secondary co-precipitation, leading to agglomeration and the rate depends on the collision force of water/ethanol molecules with the colloidal NPs (Thanh et al., 2014). Also, due to the particles' strong intrinsic magnetic interactions, they have a natural tendency to coalescence over the long aging duration (Jang et al., 2013).

Polydispersity index (PDI) is another parameter that provides information about the heterogeneity of the sample based on the particle size distribution (Rubio et al., 2019). There seems to be a direct correlation between PDI and instability index values, these measurements provide information regarding size distribution and stability (aggregation, sedimentation, and dispersion rate) in colloidal NPs systems. If PDI is high, particles will have broader size distribution, which also indicates likelihood of higher instability index values as particles aggregation, and sedimentation rate will be high. Our result showed the PDI of Fe_3O_4-pH11-80 °C-NA-ethanol (LFD, FFD, VOD and WET) were <0.3, confirming the samples had narrow particles size distribution. It also was an indicative of reduced particle aggregation.

The results for final post-treatments confirmed that the WET suspension displayed the least coagulation. Freeze-drying of the synthesised IONP after liquid-nitrogen plunge-freezing (LFD samples) showed more coagulation than the WET samples, but exhibited better dispersibility in HPLC water, compared to FFD samples (freeze-dried IONP after freezing at −4 °C), or VOD samples (vacuum-oven-dried IONP) where the particles were highly aggregated. Although, the VOD samples had smaller D_H (e.g., in VOD sample, Fe_3O_4 NPs-pH11-80 °C-NA-ethanol D_H: 125.5 nm), the dispersion was poor, the instability index was higher and the DLS graph was bi-modal/multi-modal, indicating the particles were settling swiftly. Amongst all the samples, the WET Fe_3O_4 NPs prepared using ethanol solvent at higher temperature, (80 °C) and higher pH (pH 11) with no aging had the best stability, with the narrowest size distribution. Therefore, for further characterisation and analysis of synthesised Fe_3O_4 NPs, the focus is on the synthesis conditions of pH 11 at 80 °C with no aging and the use of ethanol, in

order to explore the impact of the four different post-treatment methods (LFD, FFD, VOD and WET) in more detail.

Fig. 4(a and b) illustrates the D_H and zeta potential of the Fe_3O_4 samples (pH11-80 °C-NA-ethanol (WET, LFD, FFD, VOD)) after different post-treatment methods. The D_H, zeta potential and PDI data of the samples are also summarised in Table 1. As seen in Fig. 4(a), the WET sample had the smallest D_H (68.6 nm) while, the drying processes significantly affected the D_H and the size distribution of the samples (LFD, FFD and VOD). The VOD sample had the worst results producing three different D_H values, (92.8, 18.1, 5560 nm), a multi-modal graph, which were an indicative of high aggregation and colloidally instable sample. Also, in the case of freeze-dried samples (LFD and FFD), the variation in D_H may be attributed to the freezing condition (freezer at −4 °C which was prolonged or the fast-freezing procedure using liquid N_2) prior to freeze drying. Likewise, as seen in Fig. 4(b), the variation in zeta potential values suggest post-treatment methods considerably affected the surface charges of the particles. The zeta potential values of WET, LFD, FFD and VOD were −21 mV, −3.23 mV, +6.19 mV, and 10.7 mV respectively. WET sample showed a high stability while, different drying (vacuum/freeze drying) techniques altered surface properties of the samples (LFD, FFD, VOD), as each technique had varied drying rate. In vacuum oven drying, the water was eliminated at 60 °C, which caused high level of aggregation, leading to greater particle size, also the crystal structure of the particles may have been affected leading to compact structure, these may have affected the zeta potential of VOD sample. The freeze-drying seems caused fragility to the samples (LFD and FFD), leading to smaller and highly dispersible particles with varied surface characteristics. Consequently, this may have influenced the availability of the charges on the particles surface and affected the zeta potential.

Table 1
D_H, ZP and PDI results of Fe_3O_4 NPs-pH11-80 °C-NA-ethanol (WET, LFD, FFD, VOD).

Parameters	Fe_3O_4 NPs-pH11-80 °C-NA-ethanol			
	LFD	FFD	VOD	WET
D_H major mode (minor) (nm)	141.8	146.1, 28.2	92.8, 18.1, 5560.0	68.6
ZP major mode (minor) (mV)	6.1	-3.2	10.7	-20.8
PDI	0.21	0.33	0.23	0.20

The dispersion stability of the Fe_3O_4 NPs-pH11-80 °C-NA-ethanol (WET, LFD, FFD and VOD) were also assessed by LUMiSizer at 25 °C, 37 °C, and 43 °C, resembling ambient, normal human body and hyperthermia conditions, consecutively. As it can be seen from Fig. 4(c) for WET samples, the particles were stable at 25 °C, which is also supporting the finding by zeta potential at (25 °C). As the analysis temperature increased to 37 °C, the instability index rose. However, raising the temperature from 37 °C to 43 °C did not imply major changes, indicating the particles are stable at high temperature and can be a potential candidate for clinical applications. In contrast, the dried samples (LFD, FFD and VOD) exhibited a rise in instability index, when the temperature was increased from 36 °C to 43 °C with the LFD samples showing poorest stability at 43 °C. The poor stability could be due to the good dispersity of LFD sample

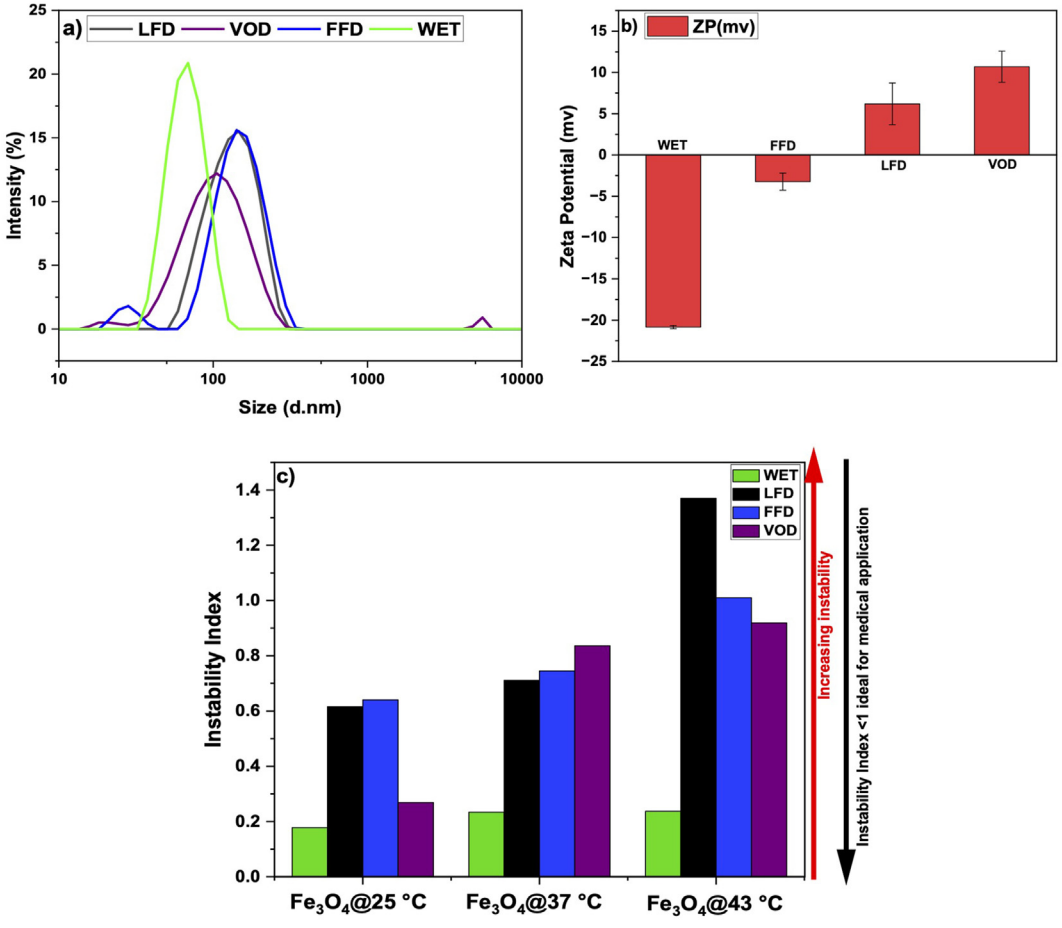

Fig. 4. (a) DLS, (b) Zeta potential, and (c) instability index measurements for Fe_3O_4 NPs-pH11-80 °C-NA-ethanol (WET, LFD, FFD, VOD).

because at elevated temperature (43 °C), the thermal energy of the highly dispersed LFD sample may have increased and the particles may have had greater kinetic energy, resulting to intensified Brownian motion and making the particles prone to agglomeration and increase of instability index.

Fig. 5(a) depicts the Fe_3O_4 NPs-pH11-80 °C-NA-ethanol (WET) crystal morphology with an average size of about 7 nm (Fig. 5(c)). The diffraction points in the selected area diffraction pattern revealed that the sample has well-defined crystallinity with inter-planer spacing of 0.26 nm. Crystal planes of (111) (220), (311), (400), (422), (511), (440), and (533) confirm the formation of Fe_3O_4 NPs (Fig. 5(b)), which align with the literature (Radoń et al., 2017). In addition, slight aggregation can be observed from the images, however, as Fe_3O_4 NPs particles are not treated with a surfactant or a coating agent, due to their intrinsic magnetic properties acceptable minor aggregation can occur.

The EDX spectra showed the chemical compositions of the sample, Fe and O peaks with high intensities and with no other impurity or contamination (Fig. 5(d), C and Cu are from TEM grids). The TEM images of Fe_3O_4 NPs-pH11-80 °C-NA-ethanol (LFD, FFD, VOD) are presented in Supplementary Fig. S1(b). It can be seen that particle morphologies are more or less similar, however the crystal size of VOD and FFD are slightly bigger than those of LFD and WET (see Table 3).

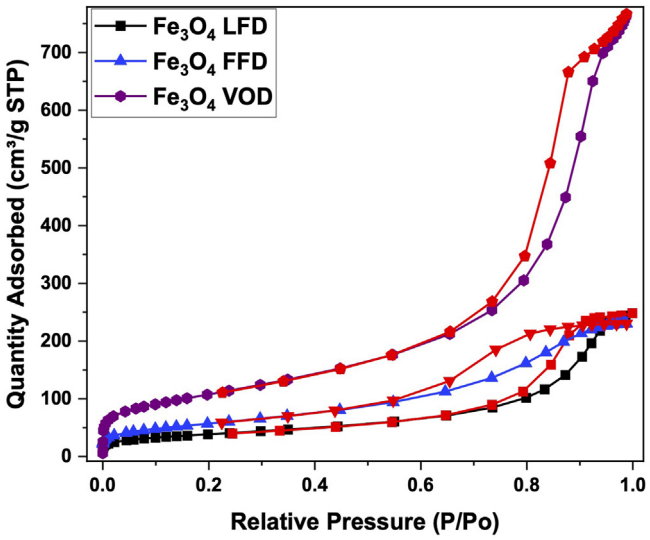

Fig. 6. BET analyses of Fe_3O_4 NPs-pH11-80 °C-NA-ethanol LFD, FFD, and VOD.

For BET, XRD, FT-IR and VSM, only dry powders were used since the available facilities could be utilized for a dry system. Fig. 6 illustrates the surface area properties of Fe_3O_4 NPs-pH11-80 °C-NA-

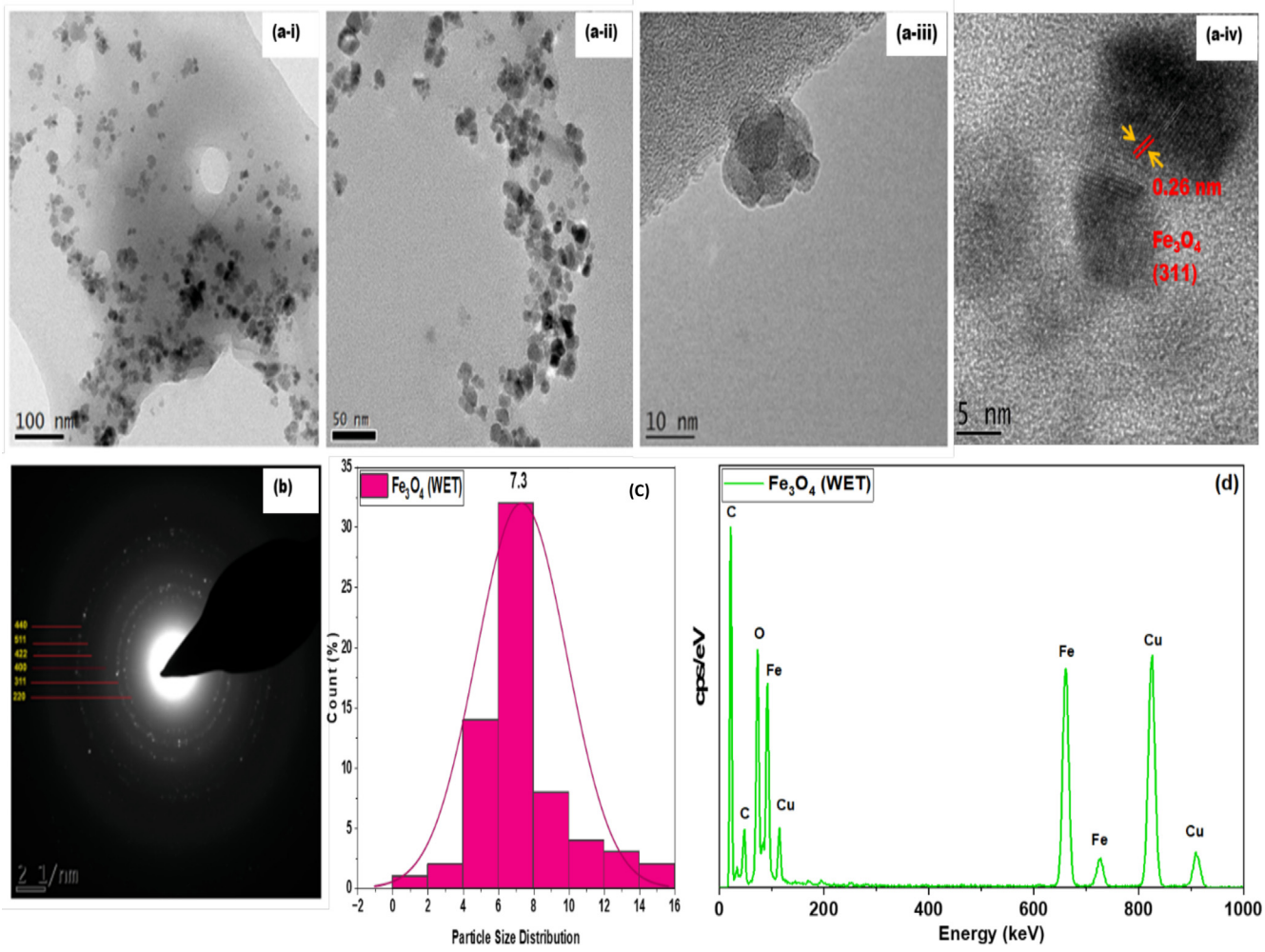

Fig. 5. (a) High-Resolution TEM images, (b) SAED Pattern, (c) d-spacing, and (d) EDX (Cu is from the cupper grid) of WET Fe_3O_4 NPs-pH11-80 °C-NA-ethanol.

ethanol (LFD, FFD, VOD) investigated by BET nitrogen adsorption-desorption measurements. Due to the wet-suspension nature, the WET sample could not be analysed by BET, so that the following results solely focus on the LFD, FFD and VOD samples. The N_2 adsorption-desorption isotherm displays the type IV(a) isotherm, which is in a good agreement with the results reported by Ambrož et al. (Ambrož et al., 2018). The hysteresis loop between the N_2 adsorption-desorption isotherm branch of the Fe_3O_4 NP samples corresponds to H1 type isotherm (according to de Boar) (Alothman, 2012; Sun et al., 2017), indicating the samples had discrete cylindrical pores or aggregate of relatively uniform spheres. According to IUPAC classifications, mesoporous materials are defined to have pore sizes between 2.0 and 50.0 nm (Tangestaninejad et al., 2009). Therefore, as it can be seen from the summery of BET analysis data which are summarised in Table 2, the samples (LFD, FFD and VOD) were mesoporous (pore size<50 nm), with the meso-porosity likely originated from the interstitial spaces between primary particles in the IONP aggregates. The VOD sample had a larger pore size and volume, compared to LFD and FFD samples, 11.9 nm, 10.8 nm, and 6.8 nm sequentially. The aggregation of VOD samples may have caused larger internal pores within the agglomerates. The surface area of Fe_3O_4 NPs, LFD, FFD and VOD samples were 139 m^2/g, 207 m^2/g, and 374 m^2/g respectively. The larger surface area in the case of the VOD sample might be due to smaller primary particle sizes.

The TEM confirmed the particles have spherical shapes; the following formula (Dallavalle, 1948) can be utilized to attain BET equivalent spherical average diameter of the primary nanoparticles.

$$D_{BET}=\frac{6000}{BET\ S.A\ (m^2/g)\times\rho_{theory}} \quad (1)$$

where D_{BET} is equivalent average diameter of spherical Fe_3O_4 NPs, *BET S.A* is the experimentally measured specific surface area, and ρ_{theory} is the theoretical density of Fe_3O_4 NPs (5 g/cm^3) (Blaney, 2007; Dallavalle, 1948). The D_{BET} values Fe_3O_4 samples are collected in Table 2. All D_{BET} values were considerably larger than the primary nanoparticle size observed by TEM (~7 nm), indicating a considerable degree of aggregation. In line with the observations on dispersion stability and hydrodynamic radius, the D_{BET} values also indicated the largest degree of aggregation for VOD sample (3.2 nm), followed by the FFD sample (5.8 nm) and LFD sample (8.6 nm).

The PXRD analysis was performed on Fe_3O_4 NPs to verify the crystallite size, and lattice structure. The PXRD showed that the d-spacing values of major peaks corresponded well with those reported in the literatures (Loh et al., 2008; Shagholani et al., 2015).The diffraction peaks at $2\theta = 18.87°, 30.60°, 36.03°, 43.65°, 53.76°, 57.76°, 63.23°$ and $74.47°$ correspond to the reflections of the (111), (220), (311), (400), (422), (511), (440) and (533) planes of Fe_3O_4, respectively, in the magnetite crystal phase, as shown in Fig. 7(a) (Aende et al., 2022; Antarnusa et al., 2020; Yazdani et al., 2016). The comparison of PXRD results with the TEM indicates that the crystal planes are consistent with TEM results reported in Fig. 5

From XRD patterns, the Scherer's equation, $D_{(311)} = K.\lambda/\beta.\cos\theta$, was used to calculate the average crystallite size (Zoleikha Hajizadeh, 2022), where $D_{(311)}$ is the crystallite size (along the (311) lattice plane of magnetite), K is the Scherrer's constant ($K = 0.94$), λ is the wavelength (CuK$\alpha = 1.54178$ Å), β is full width at half maximum of plane (311) and θ is the corresponding Bragg's diffraction angle (see the supplementary data Section S2).

The mean particle size (as determined by TEM, XRD and BET) for Fe_3O_4 NPs-pH11-80 °C-NA-ethanol after different post-synthesis processing (WET, LFD, FFD, and VOD) are compared in Table 3. XRD crystallite sizes are in excellent agreement with TEM results, indicating that the primary particles observed in TEM are single-crystalline Fe_3O_4 nano-crystals. Both TEM and XRD suggest that FFD and VOD processing lead to slightly larger primary particle sizes compared to LFD processing. In the case of FFD sample, the larger crystal size most likely could be due to the longer freezing rate (in the freezer) and drying procedure, while in VOD sample, it could be related to high drying temperature (60 °C) and Ostwald ripening. With respect to LFD sample, the small crystal size could be because of the freezing rate, as the particles were frozen by liquid N_2 in a short time and sublimed under a low pressure. This rapid temperature change (freezing and drying) could have induced stress within the particles, resulting in the reduction of Fe_3O_4 crystals size.

D_H values are noticeably larger than the primary particle sizes (as determined by TEM), indicating a significant degree of primary particle aggregation both in the dried powder form and upon re-dispersion into aqueous media. This effect is however considerably less pronounced for LFD processing, compared to FFD and especially VOD processing, likely again due to the higher temperatures and longer time scales involved in the latter two processing methods. In addition, D_H values indicate that avoiding drying altogether, by keeping IONPs as colloidal dispersion (WET sample), less aggregation will occur, in line with much better dispersion stability of the WET samples discussed earlier.

While for the LFD processing, the D_{BET} agrees well with the crystal sizes from XRD and TEM, for VOD and FFD, D_{BET} is noticeably smaller than the XRD and TEM crystal sizes. This could be due to the higher N_2 adsorption, probably due to the surface and/or internal porosities of primary particles, which leads to a higher BET surface area measurements.

The FT-IR was obtained for Fe_3O_4 NPs-pH11-80 °C-NA-ethanol (LFD, FFD and VOD), as shown in Fig. 7(b). The peak at 559.27 cm^{-1} confirms the formation of Fe-O bond which is characteristic of Fe_3O_4 IONPs species. In all samples, the broad absorption band at 3236.10 cm^{-1} and at 1631.55 cm^{-1} correspond to the vibration of O-H bonds of IONP O-H surface groups and associated surface-bound water.

Fig. 8 displays the magnetic behaviour of the Fe_3O_4 NPs-pH11-80 °C-NA-ethanol (LFD, FFD, VOD) samples under the effect of magnetic field at 300 K. The applied field was corrected against a palladium reference sample to moderate the influence of trapped flux in the superconducting magnet coil. The details are included in the supplementary section S3. The results, as summarised in Table 4, exhibited that LFD, FFD and VOD samples interestingly possessed superparamagnetic characteristics in the absence of XMF, this was supported by the negligible remanence (M_r) and low coercivity (H_c) (Chen, Ilyas, et al., 2021; Mohammadi et al., 2014). The magnetization curves were normalised to the total mass of the samples. The saturation magnetization (M_s) for LFD, FFD and VOD samples were 78.50 emu/g, 71.38 emu/g and 63.87 emu/g, respectively, as depicted in Table 4. As it is reported in literatures (Chen, Ilyas, et al., 2021; Dong et al., 2016), the effect of synthesis

Table 2
Summary of BET results of Fe_3O_4 NPs-pH11-80 °C-NA-ethanol (LFD, FFD, and VOD).

Parameters	Fe_3O_4 NPs-pH11-80 °C-NA-ethanol		
	LFD	FFD	VOD
Pore size (nm)	10.8	6.9	11.9
Pore volume (cm^3/g)	0.37	0.36	1.16
BET S.A (m^2/g)	140	208	375
Hydrodynamic size diameter D_{BET} (nm)	8.6	5.8	3.2

Table 3
Mean particle size of Fe_3O_4 NPs-pH11-80 °C-NA-ethanol (LFD, FFD, VOD and WET) by TEM, XRD, BET.

Sample description	D_H by DLS (nm)	D_{BET} by BET (nm)	D_{IONP} by TEM (nm)	$D_{(311)}$ by XRD (nm)
LFD	141.8	8.6	8.0	7.8
FFD	28.2, 146.1	5.8	10.0	10.3
VOD	18.1, 92.8, 5560.0	3.2	12.0	10.6
WET	68.6	N/A	7.0	N/A

D_{IONP}: mean diameter of primary particles as observed in TEM, D_{BET}: average particle diameter as estimated from BET surface area and Fe_3O_4 density, $D_{(311)}$ is the crystalline size. N/A: not applicable.

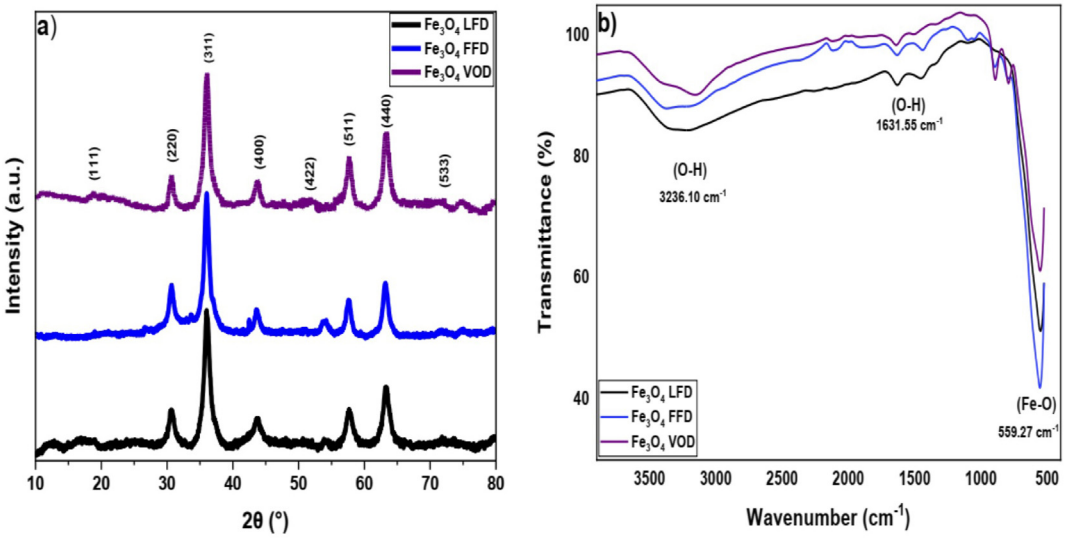

Fig. 7. (a) PXRD and (b) FT-IR spectra of Fe_3O_4 NPs-pH11-80 °C-NA-ethanol (LFD, FFD and VOD).

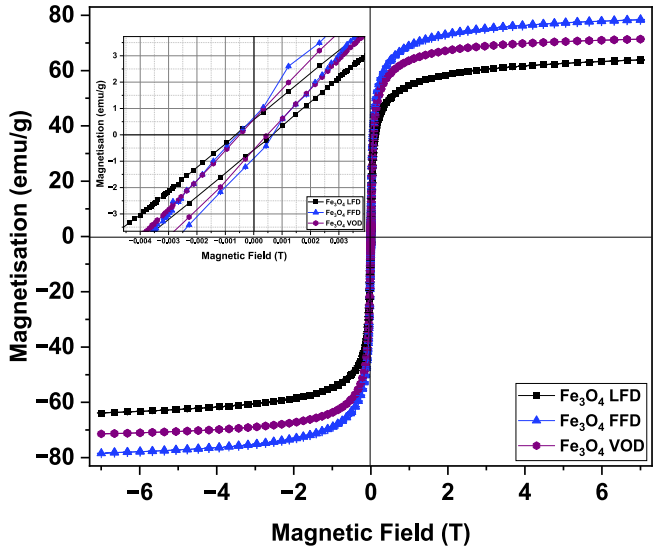

Fig. 8. Magnetization hysteresis loop of the Fe_3O_4 NPs-pH11-80 °C-NA-ethanol (LFD, FFD, VOD) at 300 K.

pathways or parameters such as concentration of iron oxide precursors, pH, temperature, size of the particles can influence the magnetic characteristics of Fe_3O_4 NPs. Herein, our work shows the post-treatment methods also can affect the magnetic properties of the samples. In comparison, between the three dried samples, LFD had the smallest particle size but greater magnetization. This could be due to the uniform size and the monodispersed particles. While,

Table 4
Magnetic properties of Fe_3O_4 NPs-pH11-80 °C-NA-ethanol (LFD, FFD, VOD) at 300 K.

Samples	LFD	FFD	VOD
H_c (T)	0.0006(2)	0.0005(3)	0.0007(2)
M_r (emu/g)	0.661(2)	0.571(5)	0.588(2)
M_s (emu/g)	78.50	71.38	63.87
M_r/M_s	0.00969	0.00801	0.00921
MPSD by TEM	8.0	10.0	12.0
B.T (K)	285	300	250

H_c: coercive field (the strength of the utilized magnetic field needed to reduce the magnetization of Fe_3O_4 NPs to zero). M_r: remnant moment (the residual magnetization in Fe_3O_4 NPs when XMF is removed. M_s: the highest magnetization. MPSD: mean particle size diameter by TEM. B.T: blocking temperature.

the VOD sample had larger particle size, with low saturation magnetization, implying the dominance of aggregation on the magnetic characteristics of the particles. In addition, the FFD sample had slightly smaller particle size compared to the VOD, hence it produced higher saturation magnetization.

Table 5 provides a comparison of effects of synthesis and post-synthesis parameters on saturation magnetism of co-precipitation synthesised Fe_3O_4 in this work and other reported literatures (Ba-Abbad et al., 2022; Mascolo et al., 2013; Shalaby et al., 2020; Shirvalilou et al., 2018; Shirzadi et al., 2020). Our findings confirmed the iron precursors, reducing agent, pH, temperature, aging, post-synthesis methods (drying/or colloidal suspension), the physico-chemistry (shape and size) can affect the saturation magnetism Fe_3O_4 NPs.

It is well-established that Fe_3O_4 exhibits ferrimagnetic properties characterized by high saturation magnetization (M_s) and low coercivity (H_c). This behaviour is attributed to the

Table 5
Comparison of D_H (nm), TEM (nm), and M_s (emu/g) of this work and other reported literatures.

Sample	Reactants	Reducing agent (%)	Temp (°C)	pH	Aging (h)	Post-synthesis process (h, °C)	D_H (nm)	TEM (nm)	Crysal size (nm)	M_s (emu/g)	Shape	Ref.
Additive-free Fe_3O_4	$FeCl_3$, $FeSO_4•7H_2O$, HPLCW, ethanol NH_4OH	25-30	80	11	N/K	WET	68.6	7.0	N/A	N/A	Sphere	This work
						LFD (48 h, −53 °C)	141.8	8.0	7.8	78.50	Sphere	
						FFD (48 h, −53 °C)	28.2, 146.1	10.0	10.3	71.38	Sphere	
						VOD (24 h, 60 °C)	18.1, 92.8, 5560.0	12.0	10.6	63.87	Sphere	
	$FeCl_3$, $FeSO_4•7H_2O$, water, ethanol, NH_4OH	30	60 ± 5	11	2	VOD (24 h, 75 °C)	N/K	10.0	8	27.35	Sphere	Ba-Abbad et al. (2022)
	$FeCl_3•6H_2O$, $FeSO_4•7H_2O$, water, ethanol, NaOH	N/A	60 ± 5	11	2	VOD (24 h, 75 °C)	N/K	32 ± 2	25	45.14	Cubic	Ba-Abbad et al. (2022)
	$FeCl_3•6H_2O$, $FeCl_2•4H_2O$, water, NH_3	25	85	N/K	N/K	WET	15	N/K	–	66.5	Sphere	Shirzadi et al. (2020)
	$FeCl_3•6H_2O$, $FeCl_2•4H2O$, water, NH_4OH	28	80	11	1/2	VOD (24 h, 70 °C)	100-300	10	–	6.07	Sphere	Shalaby et al. (2020)
	$FeCl_3•6H_2O$, $FeCl_2•4H_2O$, water, NaOH	N/A	25	12.20	3	VDr	N/K	11	10.9	69.4	Sphere	Mascolo et al. (2013)
	$FeCl_3•6H_2O$, $FeCl_2•4H_2O$, water, NH_3	25	70	N/K	2	VOD (N/K, 45 °C)	N/K	11.5	–	55.14	Sphere	Shirvalilou et al. (2018)

Temp: temperature, N/K: not known, N/A: not applicable, VDr: vacuum desiccator.

antiferromagnetic coupling of Fe^{3+} cations within the tetrahedral and octahedral sites of its crystal structure, as previously elucidated. The magnetic attributes of Fe_3O_4 iron oxide nanoparticles (IONPs), including M_s and H_c, are significantly influenced by various factors such as particle size, surface effects, magnetic ordering, temperature, and pressure (Kolhatkar et al., 2013; Lisjak et al., 2018; Lu et al., 2007). These factors, interconnected and strongly reliant on the size and geometry of the nanoparticles (NPs), contribute to the classification of Fe_3O_4 spherical IONPs based on their structures, crystallinity, and magnetic behaviours. Spherical Fe_3O_4 IONPs, particularly those with a size smaller than 25 nm and a single-crystalline structure, are identified to potentially exhibit superparamagnetic behaviour at room temperature (Kolhatkar et al., 2013; Nguyen et al., 2021), aligning with existing literature presented in Table 5. Despite the consistency in particle size and crystal structure among the compared results in Table 5, notable variations in the obtained M_s values are observed. Noteworthy is the persistent high M_s value obtained in our results compared to other reported literature, even though similar particle size and crystal structure are maintained. Additionally, it is essential to note that defects or impurities within the crystal lattice can impact the magnetic properties of Fe_3O_4 IONPs. These imperfections can disrupt the alignment of magnetic moments, introduce disorder, and consequently induce changes in saturation magnetization (Demortiere et al., 2011; Park et al., 2004). Notably, our findings suggest that the absence of the maghemite phase in the magnetite nanoparticles contributes to an increase in saturation magnetization, as proven by lattice parameters and d-spacings in Fig. 5(c). This observation is further supported by the confirmation of the dominant magnetite phase through the analysis of lattice parameters presented in Fig. 7(a). Furthermore, the qualitative presence of magnetite materials is affirmed by FT-IR results in Fig. 7(b), illustrating the formation of Fe-O bonds characteristic of Fe_3O_4 IONPs species. Overall, our study provides valuable insights into the magnetic properties of Fe_3O_4 IONPs, emphasizing the intricate interplay of various factors and highlighting the significance of crystal structure and phase composition in influencing magnetic behaviour.

The thermal hysteresis of the sample was measured. The zero-field cooled, and field cooled (ZFCFC) magnetization curve measurements started off at 400 K, de-magnetising the sample then removing the trapped flux from the superconducting magnet, followed by cooling in zero field to the base temperature (Fig. 9(a)). A very small field was then applied (~5 mT), as the temperature increased, thermal energy was applied to the Fe_3O_4 NPs to make the transition to have spin aligned with the XMF. Hence, with the rise of the temperature the magnetic moment increased too. However, susceptibility reduced after reaching the blocking temperature where the samples started to behave superparamagnetic (Martien, 2001). At 300 K, the hysteresis loops did not close and continued

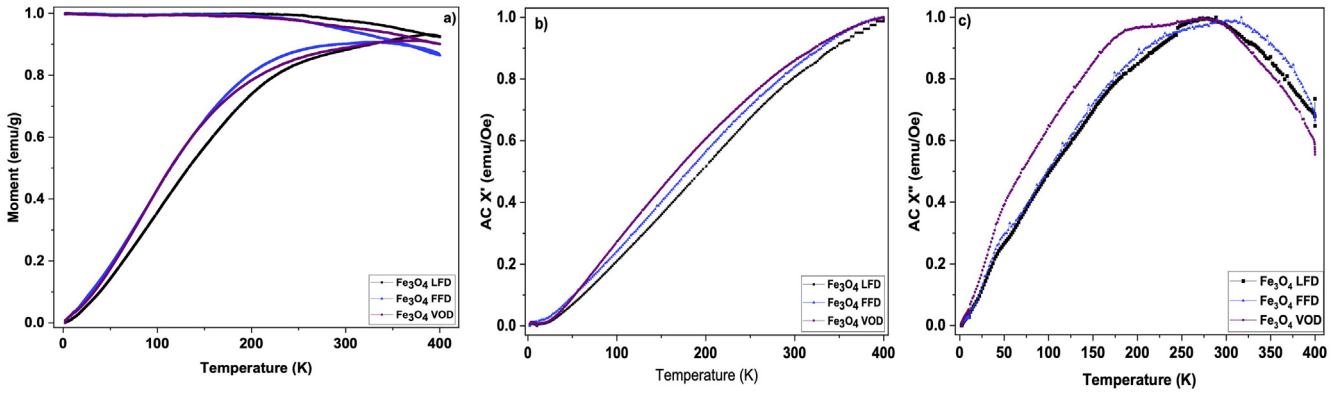

Fig. 9. Zero-field cooled, and field cooled (ZFCFC) (a), AC susceptibility, real (b), and imaginary (c) components of Fe_3O_4 NPs-pH11-80 °C-NA-ethanol (LFD, FFD and VOD).

which indicated Fe_3O_4 NPs (LFD, FFD, VOD) at a temperature between 300 K and 400 K have some ferromagnetism characteristic remaining, this might be due to the aggregation (Chen et al., 2020).

The temperature dependent AC susceptibility of Fe_3O_4 NPs-pH11-80 °C-NA-ethanol (LFD, FFD and VOD) was measured at 75.7 Hz. The AC susceptibility (c), which describes the response of Fe_3O_4 NPs powder to applied magnetic field, was measured using a dynamic oscillating magnetic field. The AC produced an in-phase or real component (c′) (Fig. 9(b)) and an out-of-phase or imaginary component (c′′) (Fig. 9(c)). The c′ and the c′′ components of the AC susceptibility illustrate the distribution of relaxation frequencies (Garaio et al., 2014). In all samples, the c′ demonstrated similar results to the static ZFCFC warming branch (Fig. 9(a)) in which with the increase of the temperature, the susceptibility increased as well. The c′ in Fe_3O_4 samples at a lower temperature started to rise gradually, indicating some of the NPs remained frozen also at a higher temperature (250 K) and slightly curved peaks were observed due to the presence of fewer spins remaining frozen.

The imaginary component provides insights about the resonance in the spin dynamic which usually shows a peak at the blocking temperature. In LFD sample, the greatest response was observed at 285 K, which indicated the narrower particle size of the sample resulted in the whole system becoming superparamagnetic after passing 285 K. While, in VOD sample prior to behaving superparamagnetic, two peaks were observed at 180 K and 250 K that could have been due to the polydispersity of the particles. Similarly, in FDD sample initially the peaks were observed at 50 K and then at 300 K prior to the system becoming superparamagnetic above this temperature.

4. Conclusion

This study revealed that in addition to the synthesis parameters, different post-synthesis treatments (LFD, FFD, VOD and WET) can also have substantial impact on particle characteristics, i.e., size, morphology, stability, magnetism, and aggregation. In terms of synthesis conditions, this work found that the Fe_3O_4 NP generated with water-ethanol solvent at 80 °C, pH 11, with no aging after reaching the desired pH, produced the best IONPs with the potential for biomedical applications (small primary particle size, homogeneous particle distribution, good dispersion stability). In terms of post-synthesis processing, this work showed, while the WET sample was less aggregated and had the smallest hydrodynamic size and the best stability at different temperatures, amongst all post-treated Fe_3O_4 NPs, the LFD samples had the smallest crystalline size with the best PDI compared to the FFD and the VOD samples. In addition, stability of post-treated samples characterised at different temperatures showed LFD is the most stable at 37 °C (body temperature), however, at 43 °C its stability significantly deteriorates. Although, freeze-dried samples had the best dispersibility among dried samples, avoiding IONPs drying and storing materials as colloidal suspension (WET) resulted in the least degree of aggregation and the best stability in aqueous dispersion at both room temperature and physiologically relevant higher temperatures. All post-treated dried samples showed superparamagnetic characteristics, however, the LFD sample had the highest saturation magnetization according to c′′ in AC susceptibility measurements.

Declaration of competing interest

The authors declare that they have no known competing financial interests or personal relationships that could have appeared to influence the work reported in this paper.

Acknowledgement

Masome Moeni would like to acknowledge the financial support from the University of Leeds through the Sanctuary Scholarship, and Mr. Alex Ferguson for his guidance and assistance. The authors also would like to thank Mr. Neil Smith, Dr. Ben Douglas, Dr. Jabbar Gardy and Dr. Christopher Pask from the University of Leeds for their technical support, and for providing training and access to the analytical equipment, and we also thank Dr. Zabeada Aslam from Leeds Electron Microscopy and Spectroscopy centre (LEMAS) for performing TEM imaging.

Appendix A. Supplementary data

Supplementary data to this article can be found online at https://doi.org/10.1016/j.partic.2024.02.006.

References

Abdelwahed, W., Degobert, G., & Fessi, H. (2006). Investigation of nanocapsules stabilization by amorphous excipients during freeze-drying and storage. *European Journal of Pharmaceutics and Biopharmaceutics: official journal of Arbeitsgemeinschaft fur Pharmazeutische Verfahrenstechnik e.V, 63*(2), 87–94.

Abdelwahed, W., Degobert, G., Stainmesse, S., & Fessi, H. (2006). Freeze-drying of nanoparticles: Formulation, process and storage considerations. *Advanced Drug Delivery Reviews, 58*(15), 1688–1713.

Aende, A., Gardy, J., Aslam, Z., Rogers, M., Edokali, M., Cespedes, O., Harbottle, D., & Hassanpour, A. (2022). *A novel highly osmotic K/Fe_3O_4/CNF magnetic draw solution for salty water desalination. Desalination, 538*(2022), Article 115903.

Aisida, S. O., Ugwu, K. C., Akpa, P. A., Nwanya, A. C., Nwankwo, U. O. A., Bashir, A. K. H., Madiba, I. G., Ahmed, I., & Ezema, F. I. (2020). Synthesis and characterization of iron oxide nanoparticles capped with Moringa Oleifera: The mechanisms of formation effects on the optical, structural, magnetic and morphological properties. *Materials Today: Proceedings, 36*(2021), 214–218.

Alothman, Z. A. (2012). A review: Fundamental aspects of silicate mesoporous materials. *Materials, 5*(12), 2874–2902.

Ambrož, F., Macdonald, T. J., Martis, V., & Parkin, I. P. J. S. M. (2018). *Evaluation of the BET theory for the characterization of meso and microporous MOFs* (Vol. 11), Article 1800173.

Antarnusa, G., & Suharyadi, E. (2020). *A synthesis of polyethylene glycol (PEG)-coated magnetite Fe_3O_4 nanoparticles and their characteristics for enhancement of biosensor. Materials Research Express, 7*(2020), Article 056103.

Ba-Abbad, M. M., Benamour, A., Ewis, D., Mohammad, A. W., & Mahmoudi, E. (2022). *Synthesis of Fe_3O_4 Nanoparticles with different shapes Through a Co-precipitation Method and their application. Journal of Occupational Medicine, 74*(9), 3531–3539.

Baojun Liu, X. H. (2020). In Q. Zhao (Ed.), *Advanced nanomaterials for pollutant sensing and environmental catalysis* (pp. 1–38). Elsevier.

Blaney, L. (2007). *Magnetite (Fe_3O_4): Properties, Synthesis, and Applications, 15*(2007), 33–81.

Boukoufi, C., Boudier, A., Maincent, P., Vigneron, J., & Clarot, I. (2022). Food-inspired innovations to improve the stability of active pharmaceutical ingredients. *International Journal of Pharmaceutics, 623*(2022), Article 121881.

Camacho, M.d. M., Egas-Astudillo, L. A., Silva, A. J. L., Uscanga, M. G. A., & Martínez-Navarrete, N. (2018). Impact of shelf temperature on freeze-drying process and porosity development. *Proceedings of 21th International Drying Symposium, 120*(2020), 143–150.

Chen, H., Billington, D., Riordan, E., Blomgren, J., Giblin, S. R., Johansson, C., & Majetich, S. A. (2020). *Tuning the dynamics in Fe_3O_4 nanoparticles for hyperthermia optimization. Applied Physics Letters, 117*(2020), Article 073702.

Chen, Y., Cheng, H., Wang, W., Jin, Z., Liu, Q., Yang, H., Cao, Y., Li, W., Fakhri, A., & Gupta, V. K. (2021). Preparation of carbon dots-hematite quantum dots-loaded hydroxypropyl cellulose-chitosan nanocomposites for drug delivery, sunlight catalytic and antimicrobial application. *Journal of Photochemistry and Photobiology B: Biology, 219*(2021), Article 112201.

Chen, F., Ilyas, N., Liu, X., Li, Z., Yan, S., & Fu, H. (2021). *Size Effect of Fe_3O_4 Nanoparticles on Magnetism and dispersion Stability of magnetic nanofluid. Frontiers in Energy Research, 9*(2021), Article 780008.

Chen, S., Zhang, Q., Nakamoto, T., Kawazoe, N., & Chen, G. (2016). Gelatin scaffolds with controlled pore structure and mechanical property for cartilage tissue engineering. *Tissue Engineering Part C Methods, 22*(3), 189–198.

Chomoucka, J., Drbohlavová, J., Húska, D., Adam, V., Kizek, R., & Hubálek, J. (2010). Magnetic nanoparticles and targeted drug delivering. *Pharmacological Research, 62*(2), 144–149.

Dallavalle, J. M. (1948). *Micromeritics : The technology of fine particles* (2 ed.). U. S. Waterways Experiment Station.

Dang, F., Enomoto, N., Hojo, J., & Enpuku, K. (2009). Sonochemical synthesis of monodispersed magnetite nanoparticles by using an ethanol-water mixed solvent. *Ultrasonics Sonochemistry, 16*(5), 649–654.

Darminto, M. N., Cholishoh, F. A., Perdana, M. A., Baqiya, M., Cahyono, Y., & Triwikantoro. (2011). *Preparing Fe_3O_4 nanoparticles from Fe^{2+} ions source by Co-precipitation process in various pH*.
Das, S. S., Bharadwaj, P., Bilal, M., Barani, M., Rahdar, A., Taboada, P., Bungau, S., & Kyzas, G. Z. (2020). Stimuli-Responsive polymeric nanocarriers for drug delivery, imaging, and theragnosis. *Polymers, 12*(6), 1397.
Demangeat, E., Pédrot, M., Dia, A., Bouhnik-Le-Coz, M., Grasset, F., Hanna, K., Kamagaté, M., & Cabello-Hurtado, F. (2018). Colloidal and chemical stabilities of iron oxide nanoparticles in aqueous solutions: The interplay of structural, chemical and environmental drivers. *Environmental Science: Nano, 5*(4), 992–1001.
Demortiere, A., Panissod, P., Pichon, B., Pourroy, G., Guillon, D., Donnio, B., & Bégin-Colin, S. (2011). Size-dependent properties of magnetic iron oxide nanocrystals. *Nanoscale, 3*(1), 225–232.
Dong, Y., Wen, B., Chen, Y., Cao, P., & Zhang, C. (2016). Autoclave-free facile approach to the synthesis of highly tunable nanocrystal clusters for magnetic responsive photonic crystals. *RSC Advances, 6*(69), 64434–64440.
Fadli, A., Amri, A., Sari, E. O., Iwantono, I., & Adnan, A. (2017). *Crystal -growth Kinetics of magnetite (Fe_3O_4) Nanoparticles using the Ostwald ripening Model. IOP Conference Series: Materials Science and Engineering, 345*(2017), 1445.
Franzé, S., Selmin, F., Samaritani, E., Minghetti, P., & Cilurzo, F. (2018). Lyophilization of liposomal formulations: Still necessary, still challenging. *Pharmaceutics, 10*(3), 139.
Garaio, E., Collantes, J.-M., Plazaola, F., García, J. A., & Castellanos-Rubio, I. (2014). A multifrequency eletromagnetic applicator with an integrated AC magnetometer for magnetic hyperthermia experiments. *Measurement Science and Technology, 25*(2014), Article 115702.
Godymchuk, A., Papina, I., Karepina, E., Kuznetsov, D., Lapin, I. N., & Svetlichnyi, V. A. (2019). Agglomeration of iron oxide nanoparticles: pH effect is stronger than amino acid acidity. *Journal of Nanoparticle Research, 21*(2019), 208.
Gommes, C. J. (2019). Ostwald ripening of confined nanoparticles: Chemo-mechanical coupling in nanopores. *Nanoscale, 11*(15), 7386–7393.
Jang, D.-H., Lee, Y.-I., Kim, K.-S., Park, E.-S., Kang, S. C., Yoon, T.-J., & Choa, Y. H. (2013). Induced heat property of polyethyleneglycol-coated iron oxide nanoparticles with dispersion stability for hyperthermia. *Journal of Nanoscience and Nanotechnology, 13*(9), 6098–6102.
Joardder, M. U. H., Karim, A., Kumar, C., & Brown, R. J. (2016). *Effect of porosity on drying kinetics and food properties*.
Kolhatkar, A. G., Jamison, A. C., Litvinov, D., Willson, R. C., & Lee, T. R. (2013). Tuning the magnetic properties of nanoparticles. *International Journal of Molecular Sciences, 14*(8), 15977–16009.
Kregar, A., Kravos, A., & Katrašnik, T. (2020). Methodology for evaluation of contributions of Ostwald ripening and particle agglomeration to growth of catalyst particles in PEM fuel cells. *Fuel Cells, 20*(4), 487–498.
Lemoine, D., François, C., Kedzierewicz, F., Préat, V., Hoffman, M., & Maincent, P. (1996). Stability study of nanoparticles of poly(epsilon-caprolactone), poly(D,L-lactide) and poly(D,L-lactide-co-glycolide). *Biomaterials, 17*(22), 2191–2197.
Lisjak, D., & Mertelj, A. (2018). Anisotropic magnetic nanoparticles: A review of their properties, syntheses and potential applications. *Progress in Materials Science, 95*, 286–328.
Loh, K. S., Lee, Y. H., Musa, A., Salmah, A., & Zamri, I. (2008). *Use of Fe_3O_4 Nanoparticles for Enhancement of biosensor Response to the herbicide 2,4-dichlorophenoxyacetic acid. Sensors, 8*, 5775–5791.
Lu, A. H., Salabas, E.e. L., & Schüth, F. (2007). Magnetic nanoparticles: Synthesis, protection, functionalization, and application. *Angewandte Chemie International Edition, 46*(8), 1222–1244.
Mahmoudi, M., Sant, S., Wang, B., Laurent, S., & Sen, T. (2011). Superparamagnetic iron oxide nanoparticles (SPIONs): Development, surface modification and applications in chemotherapy. *Advanced Drug Delivery Reviews, 63*(1–2), 24–46.
Majeed, M. I., Lu, Q.-W., Yan, W., Li, Z., Hussain, I., Tahir, M. N., Tremel, W., & Tan, B. (2013). *Highly water-Soluble magnetic iron oxide (Fe_3O_4) nanoparticles for drug delivery: Enhanced in vitro therapeutic efficacy of doxorubicin and MION conjugates. Journal of Materials Chemistry B, 1*(22), 2874–2884.
Martien, D. (2001). *Introduction to AC Susceptibility, 1*(2001), 4.
Mascolo, M. C., Pei, Y., & Ring, T. A. (2013). Room temperature Co-precipitation synthesis of magnetite nanoparticles in a large pH window with different bases. *Materials, 6*(12), 5549–5567.
Mihai, A. D., Chircov, C., Grumezescu, A. M., & Holban, A. M. (2020). Magnetite nanoparticles and essential oils systems for advanced antibacterial therapies. *International Journal of Molecular Sciences, 21*(19), 7355.
Mohammadi, A., & Barikani, M. J. M. C. (2014). *Synthesis and characterization of superparamagnetic Fe_3O_4 nanoparticles coated with thiodiglycol, 90*(2014), 88–93.
Mpelane, S., Mketo, N., Bingwa, N., & Nomngongo, P. N. (2022). Synthesis of mesoporous iron oxide nanoparticles for adsorptive removal of levofloxacin from aqueous solutions: Kinetics, isotherms, thermodynamics and mechanism. *Alexandria Engineering Journal, 61*(11), 8457–8468.
Nanda, H. S., Chen, S., Zhang, Q., Kawazoe, N., & Chen, G. (2014). Collagen scaffolds with controlled insulin release and controlled pore structure for cartilage tissue engineering. *BioMed Research International, 2014*(2014), Article 623805.
Nguyen, M. D., Tran, H.-V., Xu, S., & Lee, T. R. (2021). *Fe_3O_4 Nanoparticles: Structures, synthesis, magnetic properties, surface functionalization, and emerging applications. Applied Sciences, 11*(23), Article 11301.
Novoselova, L. Y. (2021). Nanoscale magnetite: New synthesis approach, structure and properties. *Applied Surface Science, 539*(2021), Article 148275.
Park, K. (2017). Prevention of nanoparticle aggregation during freeze-drying. *Journal of Controlled Release: Official Journal of the Controlled Release Society, 248*(2017), 153.
Park, J., An, K., Hwang, Y., Park, J.-G., Noh, H.-J., Kim, J.-Y., Park, J.-H., Hwang, N.-M., & Hyeon, T. (2004). Ultra-large-scale syntheses of monodisperse nanocrystals. *Nature Materials, 3*(12), 891–895.
Pinto, P. S., Lanza, G. D., Ardisson, J. D., & Lago, R. M. (2018). *Controlled Dehydration of $Fe(OH)_3$ to Fe_2O_3: Developing Mesopores with complexing iron Species for the Adsorption of β-lactam antibiotics. Journal of the Brazilian Chemical Society, 30*(2018), 310–317.
Priyadarshi, H., & Gaur, U. (2021). Paramagnetism-enhanced doped maghemite nanoparticles for targeted drug delivery. *Materials Today: Proceedings, 43*(2021), 3030–3033.
Radoń, A., Drygała, A., Hawełek, Ł., & Łukowiec, D. (2017). *Structure and optical properties of Fe_3O_4 nanoparticles synthesized by co-precipitation method with different organic modifiers. Materials Characterization, 131*(2017), 148–156.
Rinkel, T., Nordmann, J., Raj, A. N., & Haase, M. (2014). Ostwald-ripening and particle size focussing of sub-10 nm $NaYF_4$ upconversion nanocrystals. *Nanoscale, 6*(23), 14523–14530.
Rubio, A. L., Gómez-Mascaraque, L. G., Fabra, M. J., & Sanz, M. M. (2019). Nanomaterials for food applications: General introduction and overview of the book. *Nanomaterials for food applications A volume in micro and nano technologies*. U. S: Elsevier.
Saragi, T., Depi, B. L., Butarbutar, S. W., Permana, B., & Risdiana. (2018). The impact of synthesis temperature on magnetite nanoparticles size synthesized by co-precipitation method. *Journal of Physics: Conference Series, 1013*(2018), Article 012190.
Shagholani, H., Ghoreishi, S. M., & Mousazadeh, M. H. (2015). Improvement of interaction between PVA and chitosan via magnetite nanoparticles for drug delivery application. *International Journal of Biological Macromolecules, 78*(2015), 130–136.
Shah, S. M., Dhawan, V. V., Holm, R., Nagarsenker, M. S., & Perrie, Y. (2020). Liposomes: Advancements and innovation in the manufacturing process. *Advanced Drug Delivery Reviews, 154–155*(2020), 102–122.
Shalaby, T. I., Gawish, A. A., & Hamad, H. A. (2020). A promising platform of magnetic nanofluid and ultrasonic treatment for cancer hyperthermia therapy: In vitro and in vivo study. *Ultrasound in Medicine and Biology, 47*(3), 651–665.
Shaoqiang, Z., Dong, T., Geng, Z., Lin, H. A., Hua, Z., Jun, H., Yi, L., Minxia, L., Yaohua, H., & Wei, Z. (2018). *The influence of grain size on the magnetic properties of Fe_3O_4 nanocrystals synthesized by solvothermal method. Journal of Sol-Gel Science and Technology, 98*(2021), 1–8.
Shirvalilou, S., Khoei, S., Khoee, S., Raoufi, N. J., Karimi, M. R., & Shakeri-Zadeh, A. (2018). Development of a magnetic nano-graphene oxide carrier for improved glioma-targeted drug delivery and imaging: In vitro and in vivo evaluations. *Chemico-Biological Interactions, 295*(2018), 97–108.
Shirzadi, Z., Baharvand, H., Nezhati, M. N., & Sajedi, R. H. (2020). Synthesis of nonlinear polymer brushes on magnetic nanoparticles as an affinity adsorbent for His-tagged xylanase purification. *Colloid and Polymer Science, 298*(2020), 1597–1607.
Sun, S., Liang, F., Tang, L., Wu, J. P., & Ma, C. (2017). Microstructural investigation of gas shale in longmaxi formation, lower silurian, NE sichuan basin, China. *Energy Exploration & Exploitation, 35*(4), 406–429.
Tang, X. C., & Pikal, M. J. (2004). Design of freeze-drying processes for pharmaceuticals: Practical advice. *Pharmaceutical Research, 21*(2), 191–200.
Tangestaninejad, S., Moghadam, M., Mirkhani, V., Mohammadpoor-Baltork, I., & Ghani, K. (2009). Alkene epoxidation catalyzed by molybdenum supported on functionalized MCM-41 containing N–S chelating Schiff base ligand. *Catalysis Communications, 10*(6), 853–858.
Thanh, N. T. K., Maclean, N., & Mahiddine, S. (2014). Mechanisms of nucleation and growth of nanoparticles in solution. *Chemical Reviews, 114*(15), 7610–7630.
Vindedahl, A. M., Strehlau, J. H., Arnold, W. A., & Penn, R. L. (2016). Organic matter and iron oxide nanoparticles: Aggregation, interactions, and reactivity. *Environmental Science: Nano, 3*(3), 494–505.
Wu, K.-J., Tse, E. C. M., Shang, C., & Guo, Z. (2022). Nucleation and growth in solution synthesis of nanostructures – from fundamentals to advanced applications. *Progress in Materials Science, 123*(2022), Article 100821.
Yang, R., Ouyang, Z., Guo, H., Qu, J., Xia, J., Shen, M., & Shi, X. (2022). Microfluidic synthesis of intelligent nanoclusters of ultrasmall iron oxide nanoparticles with improved tumor microenvironment regulation for dynamic MR imaging-guided tumor photothermo-chemo-chemodynamic therapy. *Nano Today, 46*(2022), Article 101615.
Yang, L., Tanabe, K., Miura, T., Yoshinari, M., Takemoto, S., Shintani, S., & Kasahara, M. (2017). Influence of lyophilization factors and gelatin concentration on pore structures of atelocollagen/gelatin sponge biomaterial. *Dental Materials Journal, 36*(4), 429–437.

Yazdani, F., & Seddigh, M. (2016). Magnetite nanoparticles synthesized by co-precipitation method: The effects of various iron anions on specifications. *Materials Chemistry and Physics, 184*(2016), 318–323.

Yusoff, A. H. M., Salimi, M. N. A., & Jamlos, M. F. (2018). Critical parametric study on final size of magnetite nanoparticles. *IOP Conference Series: Materials Science and Engineering, 318*(2018), Article 012020.

Zhao, X., Xu, S., Jiang, Y., Wang, C., ur Rehman, S., Ji, S., Wang, J., Tao, T., Xu, H., Chen, R., Cai, Y., Jiang, Y., Wang, H., Ma, K., & Wang, J. (2023). BSA-magnetite nanotorpedo for safe and efficient delivery of chemotherapy drugs. *Chemical Engineering Journal, 454*(2023), Article 140440.

Zoleikha Hajizadeh, R. T.-L. (2022). Preparation and synthetic methods. In A. Maleki (Ed.), *Heterogeneous micro and nanoscale composites for the catalysis of organic reactions* (pp. 23–31). Elsevier.